THE JOURNAL OF PHYSICAL CHEMISTRY C

Article

pubs.acs.org/JPCC

Direct Comparison of Second Harmonic Generation and Two-Photon Photoluminescence from Single Connected Gold Nanodimers

Jiyong Wang,[†,‡,§] Jérémy Butet,[∥] Anne-Laure Baudrion,[‡] Andreas Horrer,[§,⊥] Gaëtan Lévêque,[#] Olivier J. F. Martin,[∥] Alfred J. Meixner,[†,§] Monika Fleischer,[§,⊥] Pierre-Michel Adam,*[,‡] Anke Horneber,[†,§] and Dai Zhang*[,†,§]

[†]Institute of Physical and Theoretical Chemistry, Eberhard Karls University of Tübingen, Auf der Morgenstelle 15, 72076 Tübingen, Germany

[‡]Laboratoire de Nanotechnologie et d'Instrumentation Optique, ICD, CNRS UMR 6281, Université de Technologie de Troyes, 12 Rue Marie Curie, CS42060, 10004 Troyes Cedex, France

[§]Center for Light-Matter-Interaction, Sensors and Analytics (LISA[+]), Eberhard Karls University of Tübingen, Auf der Morgenstelle 15, 72076 Tübingen, Germany

[∥]Nanophotonics and Metrology Laboratory (NAM), Swiss Federal Institute of Technology, Lausanne (EPFL), 1015 Lausanne, Switzerland

[⊥]Institute for Applied Physics, Eberhard Karls University of Tübingen, Auf der Morgenstelle 10, 72076 Tübingen, Germany

[#]Institut d'Electronique, de Microélectronique et de Nanotechnologie (IEMN, CNRS-8520), Cité Scientifique, Avenue Poincaré, 59652 Villeneuve d'Ascq, France

Supporting Information

ABSTRACT: In this article we compare the two-photon photoluminescence and second harmonic generation from single connected gold nanodimers. Analyzing the particle size-dependent nonlinear optical spectra and performing excitation polarization resolved measurements using an experimental setup combining a femtosecond laser source with a parabolic mirror, we show that second harmonic generation and two-photon photoluminescence have different behaviors despite the same expected fundamental intensity-dependence. For further understanding of the observed phenomena, the plasmon resonances of single nanodimers are investigated using dark-field optical microscopy, and calculations are performed with Green's tensor method. Furthermore, the underlying mechanisms explaining the differences between these two optical processes are investigated using a surface integral equation method for the nonlinear computations. This study reveals that the different trends in the polarization-dependences of two-photon photoluminescence and second harmonic generation with the increasing diameters of the connected discs are due to their distinct physical nature, resulting in specific rules for plasmon enhancement and different coherence properties. Furthermore, this article clearly points out that special care has to be taken when two-photon photoluminescence and second harmonic generation are used to evaluate the amplitudes of electromagnetic hot-spots generated in plasmonic nanostructures.

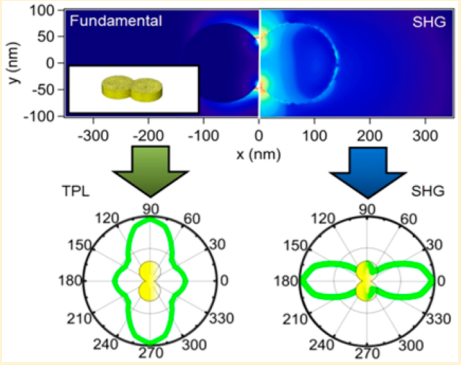

INTRODUCTION

Plasmonic nanoantennas, exhibiting fascinating linear and nonlinear optical properties, have been the subjects of numerous investigations in the recent years.[1−5] Their potential applications in a variety of fields, ranging from biosensing,[6−8] to light harvesting systems,[9,10] to field effect transistors,[11,12] have motivated researchers to understand the fundamental physical properties and the optical processes that occur in plasmonic nanoantennas. Localized surface plasmon resonances (LSPRs) have attracted particular attention as they allow enhancing and concentrating the electromagnetic field in subwavelength volumes.[5,13−19] The influences of LSPRs on the linear optical properties of plasmonic nanoantennas, such as scattering, absorption, and one-photon photoluminescence emission, have been rigorously investigated.[20−27] To study the electromagnetic field amplitude in the so-called optical hot-spots, corresponding to the areas where the incident field intensity is enhanced by some orders of magnitude, researchers relied on several spectroscopic techniques such as photoluminescence emission from the metallic nanostructures,[28−30] fluorescence or Raman signals from molecules that are immobilized at the nanoantenna surface,[31−33] and also electron energy loss spectroscopy

Received: May 13, 2016
Revised: July 8, 2016
Published: July 8, 2016

DOI: 10.1021/acs.jpcc.6b04850
J. Phys. Chem. C 2016, 120, 17699−17710

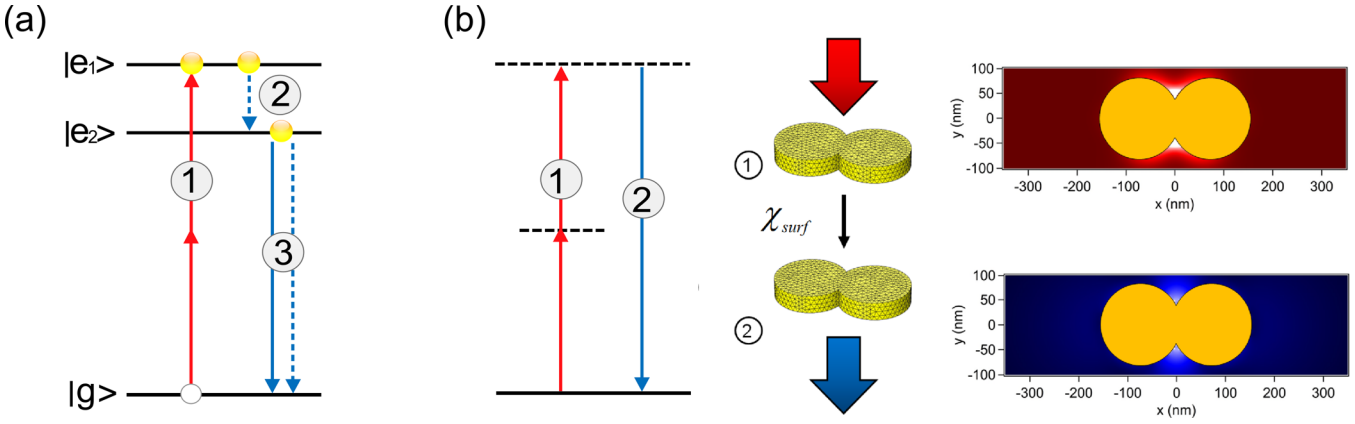

Figure 1. (a) Energy level diagram for TPL. The complete process consists of three steps: excitation step, relaxation step, and emission step. In the first step, an electron from the ground state $|g\rangle$ is promoted to the excited state $|e_1\rangle$ by absorbing two photons from a femtosecond (fs) laser pulse, creating a hole in the ground state. Once thermal equilibrium is reached (step 2), the electron in the excited state $|e_2\rangle$ decays (step 3) either radiatively in terms of photoluminescence (solid arrow) or nonradiatively in terms of heat dissipation (dashed arrow). (b) Energy level diagram for SHG. In comparison to TPL, SHG is a parametric process involving virtual states (indicated as dashed horizontal lines), corresponding to the destruction of two fundamental photons followed by the generation of one SH photon. Classically, the fundamental near-field driven by the incoming wave induces a nonlinear surface polarization $P_{surf,n}(\mathbf{r}, 2\omega)$ due to the nonlinear surface susceptibility χ_{surf} (step 1). The second step is the electromagnetic radiation of the nonlinear sources. As an example, the near-field intensities of a connected dimer with a diameter of 160 nm at the fundamental and the SH frequencies are shown in red and blue, respectively.

(EELS).[34,35] More recently, the observation of nonlinear optical processes in plasmonic nanoantennas has started to attract increasing attention.[1,36,37] Indeed, various nonlinear optical processes, such as second harmonic generation (SHG), two-photon photoluminescence (TPL), third (THG) and higher harmonics generation, as well as multiphoton photoluminescence, have been investigated.[38−46] In comparison to linear optical processes, the generation of nonlinear optical signals requires a much higher excitation field.[47] Plasmonic nanoantennas can be used for the excitation of these optical processes since the field intensity at the fundamental wavelength is increased in their vicinities thanks to the LSPR. This enhancement is expressed by the local field factor $L(\omega)$, which is defined as the amplitude ratio between the local electric field and the incident electric field at the frequency ω. Since the conversion yield of nonlinear optical processes varies nonlinearly with the fundamental intensity, this conversion yield might be expected to increase with the fourth or a higher power with the local field factor $L(\omega)$ evaluated at the fundamental frequency. For this reason, it was proposed to use nonlinear optical processes to accurately measure the field enhancement in electromagnetic hot-spots, e.g., nanogaps, taking advantage of this nonlinear dependence.[48,49] However, such a description of nonlinear optical processes in plasmonic nanoantennas is somewhat limited. For example, due to the specific selection rules, the SHG from tiny centrosymmetric nanogaps is weak,[50−53] despite a strong fundamental field enhancement. As a consequence, the relationships between the field enhancement and the conversion yields of the various nonlinear optical processes need to be carefully determined and mastered, before they can be safely used for characterizing the magnitude of the electromagnetic field in hot-spots.

In this article, we discuss the influence of the local near-field intensity distribution on the excitation and emission processes of TPL and SHG, by varying the plasmon resonance of the nanostructures and the polarization of the incident beam, on a model system consisting of connected circular dimers. Analyzing the single particle emission spectra and excitation polarization resolved measurements with the assistance of a surface integral equation (SIE) method, we show that, despite the same fundamental intensity-dependence, SHG and TPL exhibit different behaviors due to their coherence properties, rules for plasmon enhancement, and the amplitude of the local near-field. It is well-known that TPL is a third order effect, associated with two-photon absorption, whereas SHG is a second order nonlinear optical effect. Both are, however, quadratically dependent on the laser intensity despite different physical origins.[30,54−57] TPL is usually described as follows;[13,57−59] see Figure 1a. The complete process consists of three steps: namely, the excitation step, relaxation step, and emission step. In the first step, an electron from the ground state $|g\rangle$ is promoted to the excited state $|e_1\rangle$ by absorbing two photons from a femtosecond (fs) laser pulse, creating a hole in the ground state. Once thermal equilibrium is reached (step 2), the electron in the excited state $|e_2\rangle$ decays (step 3) either radiatively in terms of photoluminescence (solid arrow) or nonradiatively in terms of heat dissipation (dashed arrow). The excitation step of TPL is a third order two-photon absorption (TPA) process (see Supporting Information, Figure S1). These different steps result in a broadband emission at wavelengths longer than the second harmonic (SH) wavelength. On the other hand, SHG is a parametric process involving virtual states, corresponding to the destruction of two fundamental photons followed by the generation of one SH photon, as shown in Figure 1b. Classically, the fundamental near-field driven by the incoming wave induces a nonlinear surface polarization $P_{surf,\perp}(\mathbf{r}, 2\omega)$ (component normal to the surface) due to the nonlinear surface susceptibility χ_{surf} (step 1). The following step is the electromagnetic radiation of the nonlinear sources located at the nanoparticle surface (step 2). The near-field intensities of a connected dimer with a diameter of 160 nm at the fundamental and the SH frequencies are shown on the right of Figure 1b as an example. SHG is visible in the nonlinear emission spectra as a narrow peak centered exactly at half the fundamental wavelength. Both optical processes have been proposed for deriving the intensity of electromagnetic hot-spots in plasmonic nanostructures by taking advantage of their quadratic dependence on the incident power.[1,36,48,49] We will discuss in the

DOI: 10.1021/acs.jpcc.6b04850
J. Phys. Chem. C 2016, 120, 17699−17710

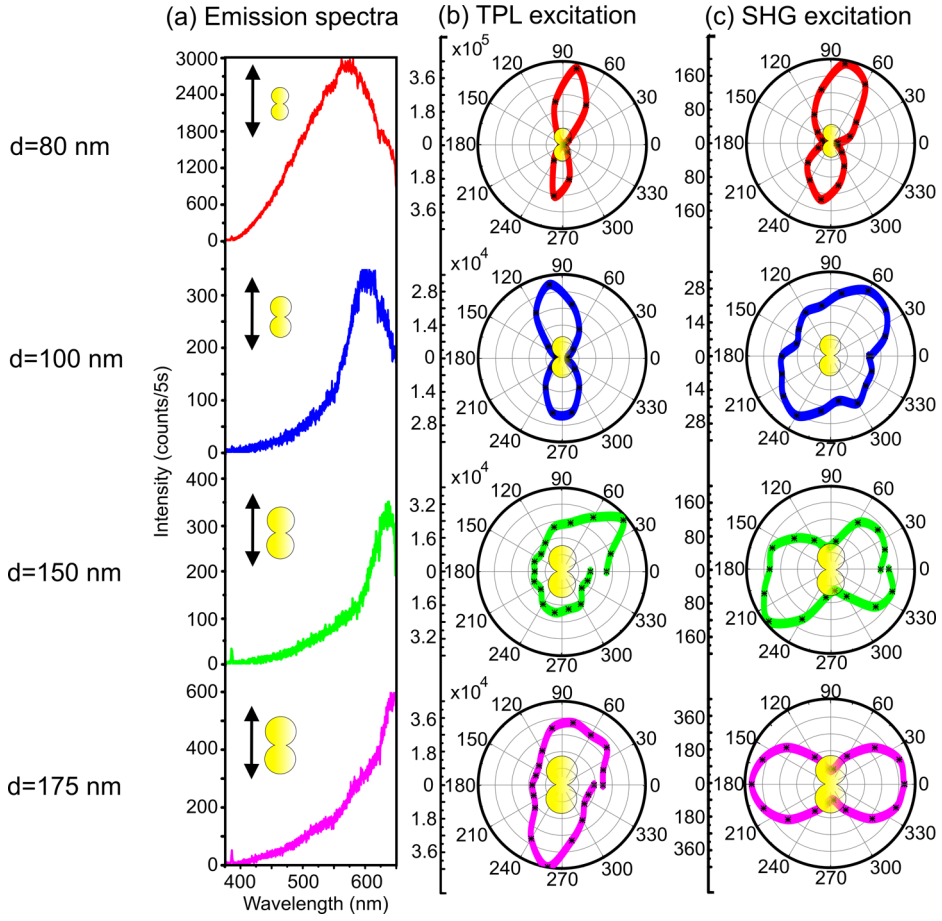

Figure 2. (a) Emission spectra, (b) TPL signals, and (c) SHG signals as a function of the different excitation polarizations for single connected gold nanodimers with nanoparticle diameters d = 80, 100, 150, and 175 nm, respectively. In panel a, the nonlinear spectra were recorded for an incident polarization along the long dimer axis, as represented by the black arrows in the insets. In panels b and c, the starting polarization angle (0°) is perpendicular to the long dimer axis. Excitation laser: 774 nm (110 fs, 89 MHz). Polarization: linearly polarized beam.

following the different dependences of TPL and SHG on the enhanced near-field intensity and incident polarization.

RESULTS AND DISCUSSION

To study the influence of the dimer geometry on the SHG and TPL signals, arrays of connected nanodimers composed of discs with different diameters (d = 80, 100, 150, and 175 nm) were fabricated using electron-beam lithography followed by lift-off. An SEM image of a connected single nanodimer is shown in the Supporting Information (Figure S2). Gold monomers (d = 80 and 100 nm) were also fabricated to serve as references. The spacing between the individual nanostructures is 10 μm such that the dark-field scattering measurements and the nonlinear optical measurements can be performed at a single particle level with confocal microscopy. The structure height is 50 nm. A detailed description of the fabrication procedure as well as the setups used for the linear and nonlinear optical measurements can be found in the Methods section. A sketch of the optical microscope used for the nonlinear measurements is included in the Supporting Information (Figure S2).

To study the role of the LSPRs for the SHG and TPL signals from the nanodimers, polarization-dependent measurements are performed by rotating the incident linear polarization using a half wave plate that is positioned in the excitation path. As an example, the spectra recorded for an incident wave polarized along the long axis of a single dimer are shown in Figure 2a. A weak and narrow peak situated at 387 nm is observed, which corresponds to SHG, and the width of which is related to the bandwidth of the femtosecond pulses. The second observed feature is an intense and broad peak, with a maximum at longer wavelengths than the SH peak and moving to lower energies as the diameter of the connected nanodisc increases. This nonlinear emission corresponds to the TPL signal that shows a second order power-dependence (Figure S3 in the Supporting Information). These spectral observations are in agreement with the mechanisms discussed in Figure 1. In order to quantify the influence of the incident polarization on the TPL and SHG signals, we integrated the intensities from 380 to 390 nm (after subtraction of the TPL background) for the SH intensity and from 390 to 650 nm for the TPL for each incident polarization angle. The incident polarization was rotated with a step of 20°. Polarization-dependent intensities of TPL and SHG from connected dimers with different sizes are shown in Figure 2b,c, respectively. Different behaviors of the TPL and SHG are clearly observed. Independent of the nanodimer size, the maxima of the TPL polarization-dependence plots are always obtained when the incident laser beam is polarized along the long dimer axis. The maxima of the SHG polarization-dependence plots, however, vary with the particle size. For the smallest dimers, i.e., d = 80 and 100 nm, the maxima of the SHG polarization-dependence plots are reached for an incident laser beam polarized along the long dimer axis, as observed in

DOI: 10.1021/acs.jpcc.6b04850
J. Phys. Chem. C 2016, 120, 17699−17710

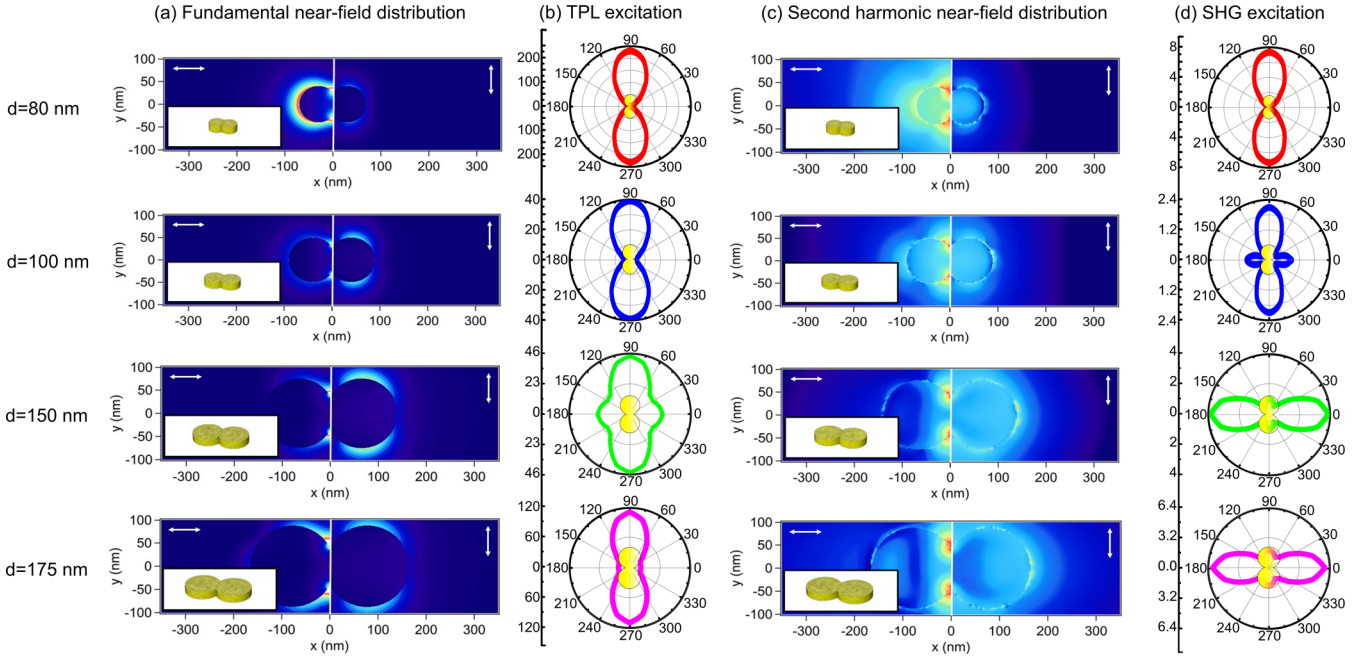

Figure 3. (a) Near-field intensity distributions at the fundamental wavelength around connected nanodimers with different disc diameters calculated using the SIE method. The left panel shows the field distributions for the incident wave polarized along the long dimer axis, while the right panel indicates the situations for the excitation polarization along the short dimer axis. The polarization direction is shown as a white arrow. For simplicity, the field distribution around only half of the nanodimer is shown in each panel. (b) The corresponding TPL signals as a function of the excitation polarizations computed with the SIE method (see Methods section). (c) Near-field distributions at the SH wavelength around connected nanodimers with different disc diameters. The polarization direction is shown as a white arrow. (d) The corresponding SHG signals as a function of the different excitation polarizations computed with the SIE method (see Methods section). The disc diameters are d = 80, 100, 150, and 175 nm, respectively. The near-field distributions within panels a and c are each plotted with the same color scale. In panel a, a linear scale is used, and in panel c, a log scale is employed for the SH near-field intensities.

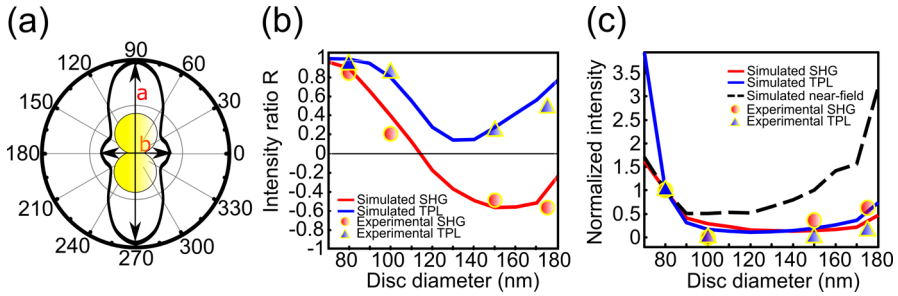

Figure 4. (a) Intensity ratio R is defined as $(a - b)/(a + b)$, where a and b are the axial intensity values in the polar excitation plots along the long dimer axis and the short dimer axis, respectively. (b) The intensity ratios R are plotted for SHG and TPL as a function of the disc diameter d. The parameter R was evaluated from both the simulation (solid lines, steps of 10 nm) and experimental results (red dots for SHG and blue triangles for TPL). (c) The different dependences of the simulated far-field SHG (red solid line), far-field TPL (blue solid line), and fundamental near-field intensity (corresponding to the maximum of the external fundamental intensity enhancement observed close to the junction between the two nanoparticles for x = 0 nm, black dashed line) on the diameters of the discs. The incident wave is polarized along the long dimer axis for both the experimental and theoretical results. The experimental SHG and TPL signals are derived from their respective maximum intensities shown in Figure 2a, which are marked as red dots and blue triangles, respectively. All the data are normalized to the corresponding ones obtained for a disc diameter d = 80 nm.

the case of TPL. On the other hand, for the largest dimers, i.e., d = 150 and d = 175 nm, the maxima flip by about 90°, and SHG is maximized when the incident wave is polarized along the short dimer axis. For the large dimers, the excitation angle resolved nonlinear emission plots do not precisely start and end at the same point, which may be due to minor variations in the rotating angles of the λ-half wave plate or slight reshaping of the dimers during the measurements. The different evolutions of the TPL and the SHG signals recorded from the same single nanostructures point out that it is not always straightforward to derive the orientation of a nanodimer only from its incident field polarization-dependent far-field SHG intensity.[52]

To understand this particular behavior, and discuss the differences between TPL and SHG, simulations were performed using the SIE method. For SHG of metallic nanoparticles, the component $\chi_{surf\perp\perp\perp}$ (where $\perp$ denotes the component normal to the surface) of the surface tensor creates the dominant contribution.[60,61] Other contributions, such as the tangential component of the surface tensor as well as bulk contributions, contribute weakly to the total SH response.[53,54,60,61] On the other hand, the TPL intensity resulting

DOI: 10.1021/acs.jpcc.6b04850
J. Phys. Chem. C 2016, 120, 17699−17710

from a pumping beam with a fundamental frequency ω_1 is given by[62] $I_{TPL} = \int \eta(\omega_2)|L^2(\omega_2)|\, d\omega_2 \cdot \int\int\int |E(r, \omega_1)|^4\, dV$, where ω_2 is the frequency of the TPL signal, $\eta(\omega_2)$ is the intrinsic luminescence yield of gold that is related to its electronic band structure, and $L(\omega_2)$ is the local field factor at the emission frequency. More details about the simulation can be found in the Methods section. Numerical results for the different connected dimers are shown in Figure 3, where panels a and c present the near-field intensities at the fundamental and SH frequencies, and panels b and d the far-field TPL and SHG intensities obtained for different incident polarizations. In a comparison of the excitation polarization-dependences of TPL and SHG shown in Figures 2 and 3, very good agreement between the simulations and experiments is clearly seen. Indeed, the highest TPL intensities are always obtained by polarizing the incident beam along the long dimer axis as shown in Figure 3b, and a flip of the polarization-dependence of SHG as the nanoparticle size increases is also predicted, as shown in Figure 3d.

For an illustration of the gradual evolutions of the polarization-dependences as the nanodimer size changes, simulations have been performed for connected dimers with disc diameters ranging from 70 to 180 nm with a 10 nm step width. As shown in Figure 4a, an intensity ratio $R = (a - b)/(a + b)$ is introduced to quantify the orientation of the polar plots that represent the excitation polarization-dependences of the SHG and TPL signals, where a and b are the axial intensity values in the polar excitation plots along the long dimer axis and the short dimer axis, respectively. A positive R indicates that the optical signal maximum is observed by polarizing the incident wave along the long axis, while a negative R stands for a maximum obtained by polarizing the incident wave along the short axis. With this definition, a change in the sign of R describes a "flip" of the intensity ratio between a and b in the excitation polarization-dependence plot. As can be seen from the blue curve in Figure 4b, the parameter R associated with the simulated TPL signal varies with the nanoparticle diameter. Notably, the parameter R is positive for all the studied particle sizes, indicating that the TPL signal is always maximized by polarizing the incident beam along the long dimer axis, whatever the connected dimer size. In the case of SHG, the sign of R changes from positive to negative values as the nanoparticle diameter increases, as shown by the red curve in Figure 4b, reproducing the "flipping" phenomenon. These trends agree very well with the intensity ratio R derived from the experimental results, as shown in Figure 4b. The different dependences of the near-field SHG and TPL signals on the nanoparticle sizes are further demonstrated in Figure 4c. The simulated fundamental near-field intensity corresponds to the maximum of the external fundamental intensity enhancement observed close to the junction between the two nanoparticles. The experimental SHG and TPL are taken from the maximum intensities of the nonlinear spectra shown in Figure 2a. The incident wave is polarized along the long dimer axis for both the experimental and theoretical results. All the data are normalized to the corresponding ones obtained for a disc diameter d = 80 nm. As one can clearly see, the SHG and TPL signals are not proportional to the square of the fundamental near-field intensity observed close to the connection between the nanoparticles.

To interpret the different evolutions of the intensity ratio R for SHG and TPL as the nanoparticle diameter increases, we now turn our attention to the plasmonic resonances supported by the connected dimers. Single particle dark-field optical spectroscopy was employed to record the scattering spectra of the dimers, the nonlinear responses of which have been discussed so far. The measured scattering spectra are shown in Figure 5a,b, while the corresponding numerical calculations

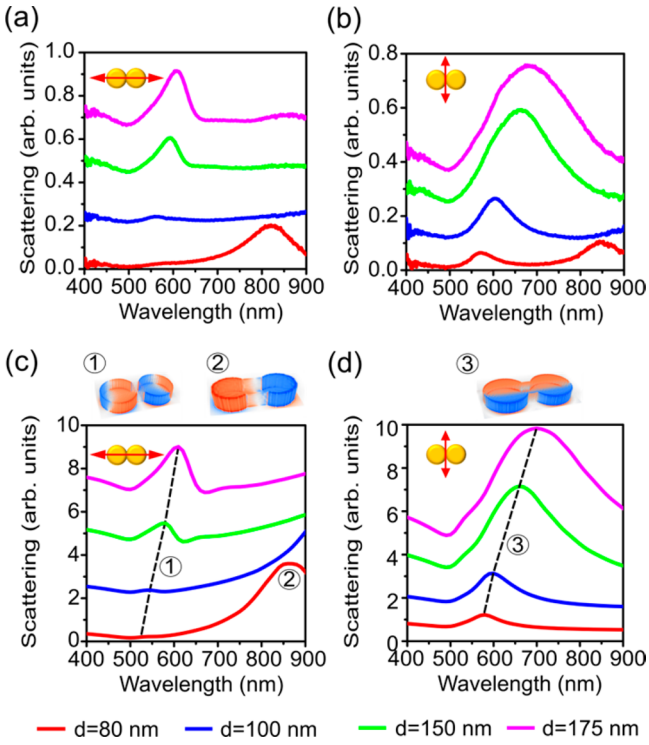

Figure 5. (a, b) Measured dark-field scattering spectra of connected gold dimers with different disc diameters: d = 80 nm (red), 100 nm (blue), 150 nm (green), and 175 nm (magenta). The intensity is normalized to the lamp spectrum. (c, d) Corresponding numerical calculations performed using Green's tensor method. The incident polarizations are depicted in the insets as red arrows. The charge distributions associated with the different observed LSP modes are labeled 1, 2, and 3. They correspond to the modes resulting from hybridization between quadrupolar modes, longitudinal dipolar modes, and transverse dipolar modes, respectively. The dashed lines in panels c and d highlight the shift of the LSPRs with the nanoparticle size. All the spectra are offset vertically for a better visibility.

performed using the Green's tensor method are shown in Figure 5c,d. The details about the microscope configuration and simulation can be found in the Methods section and Supporting Information. The incident polarization is oriented either along the long axis or the short axis as depicted in the insets. Good agreement between the experimental and numerical spectra is clearly observed. In the case of the longitudinal excitation, two different maxima are observed in the scattering spectra as shown in Figure 5a,c. The first mode appears between 500 and 610 nm corresponding to the coupling between two quadrupolar modes, in accordance with the charge distribution 1 shown in Figure 5c. As seen in Figure 5a,c, this mode shifts from ~550 nm for a disc diameter d = 100 to 607 nm (610 nm in the simulation) for d = 175 nm. The second mode, which resonates at a wavelength around 820 nm for the smallest diameters, is a longitudinal dipolar mode. It corresponds to charge oscillations along the long dimer axis, the charge distribution of which can be seen in Figure 5c as 2. As the diameter increases, this mode shifts to longer wavelengths

DOI: 10.1021/acs.jpcc.6b04850
J. Phys. Chem. C 2016, 120, 17699−17710

beyond the spectral range detectable with our experimental setup. For incident light polarized along the short dimer axis, a transverse dipolar mode between 570 and 680 nm is observed, corresponding to charge oscillations along the short dimer axis as revealed by the charge distribution in Figure 5d. This mode also red-shifts as the disc diameter increases but remains detectable with our dark-field microscope. This plasmonic mode shifts from 570 nm for a disc diameter of d = 80 to 677 nm for d = 175 nm. A small peak at about 850 nm appears for the smallest dimer when the light is polarized along the short axis, which does not appear in the simulation. It may originate from a slight misalignment of the incident polarization relative to the dimer's short axis during the scattering measurements.

With the knowledge of the plasmon resonance properties of the connected nanodimers, the enhancement of the nonlinear signals via the different surface plasmon modes can be well-understood. First, despite the lowest volume, the dimer with the smallest disc diameter (d = 80 nm) has the strongest TPL signal. This observation is related to the property that its longitudinal dipolar mode occurs close to the fundamental excitation wavelength (774 nm), as can be seen from the red curves in Figure 5a,c. As a consequence of this resonant excitation, a strong near-field enhancement is observed close to the dimer, in particular at the touching points between the nanodiscs, when the incident wave is polarized along the long axis, see Figure 3a. On the contrary, only a weak near-field enhancement is generated when the incident wave is polarized along the short dimer axis. As the TPL signal is proportional to the fourth power of the electric field at the fundamental frequency, the efficient excitation of the TPL with the polarization along the long dimer axis for the small dimer can be easily understood, see also Figure 4c.

As the disc diameter increases, the longitudinal dipolar mode shifts to longer wavelengths. Therefore, larger dimers are no longer resonantly excited by the incident light resulting in a smaller TPL signal than the one observed from the connected dimer with disc diameter d = 80 nm. Note that, for these cases, a stronger near-field enhancement is still achieved via an incident polarization along the long dimer axis than that along the short axis. This is due to the generation of electromagnetic hot-spots between the two nanoparticles, close to the nanodisc touching points as shown in Figure 3a for d = 100, 150, and 175 nm. In these cases, with longitudinal polarization excitation, the electric fields in the hot-spots are parallel to the dimer connections, and the electric field can penetrate into the gold dimers resulting in strong two-photon absorption. On the contrary, when the incident wave is polarized perpendicular to the long dimer axis, the local electric field is mainly orthogonal to the nanoparticle surface and the internal field is somewhat reduced by the electron screening limiting the two-photon absorption. Therefore, despite the particle size differences, no "flip" of the TPL polarization-dependence plot is observed, and the TPL maximum is always achieved with the incident polarization along the long dimer axis.

Contrary to the TPL signal, the SHG polarization-dependence changes with the disc diameter as confirmed by both the experimental and simulated results shown in Figures 2 and 3. To understand this "flip" of the intensity ratio between a and b, both the plasmon resonance and the polarization of the local near-field at the electromagnetic "hot-spot" should be considered. For the dimer with disc diameter d = 80 nm, strong near-fields at both the fundamental and the SH frequencies are observed around the dimer, due to the resonant excitation of the longitudinal dipolar mode at the fundamental wavelength. Therefore, the maximum SHG intensity is achieved for an incident wave polarized along the long dimer axis. As the disc diameter increases, the resonance of the longitudinal dipolar mode moves further away from the excitation wavelength. On the other hand, the resonance of the transverse dipolar mode approaches gradually toward the fundamental wavelength as seen in Figure 5d. The direct consequence is that the excitation efficiency of the transverse dipolar mode is clearly improved, see Figure 3c. At the SH frequency, the near-field intensities around the dimers increase gradually as the disc diameter evolves from d = 100 to 175 nm, for an incident polarization along the short dimer axis. This fundamental electric field is mainly perpendicular to the nanoparticle surface and drives strong SH sources through the $\chi_{surf,\perp\perp\perp}$ component of the nonlinear surface susceptibility, which is the dominant contribution to the SHG of metallic nanoparticles.[60,61] At the end, it outweighs the near-field strength generated with an incident polarization along the long axis. Therefore, the SHG polarization-dependence plots "flip" as the particle size increases. Notably, for dimers with disc diameters d = 150 and 175 nm, although strong electromagnetic "hot-spots" at the SH frequencies can be observed around the touching points between the nanodiscs when the incident wave is polarized along the long axis, the SHG intensity is smaller than for the polarization along the short axis. This phenomenon has been reported as the "silencing" of the second order nonlinear response.[50,53,63] Although a strong near-field enhancement is present, the nonlinear polarization vectors at each side of the touching point are out of phase, and their contributions to the far-field SH wave tend to cancel each other out, see Figure S4 in the Supporting Information. The destructive interference finally results in a limited far-field SH signal, despite the amplitude of the nonlinear surface polarization. Note that this "silencing" effect is present in all the connected dimers, but results in a "flip" of the SH response only if the SHG for an incident wave polarized along the short dimer axis is high enough, i.e., for large disc diameters. This observation indicates that the measurement of electromagnetic hot-spots using nonlinear optical processes is not direct, because a competition between different enhancement mechanisms of the nonlinear response often occurs, meaning that a careful description of the underlying mechanisms is required. In other words, the numerical simulations do not only support our experimental results, but also provide an insight into the difference between TPL and SHG. Despite the fact that the efficiency of these two nonlinear optical processes scales with the incident intensity squared, their physical origins are obviously different. As discussed above, TPL is an incoherent optical process involving the absorption and inelastic emission from the bulk of plasmonic nanostructures, while SHG is a coherent optical surface process. Due to their distinct physical nature, TPL and SHG do not evolve in the same manner with the near-field distribution. This is a critical point because both optical processes have been proposed to record the intensity of electromagnetic hot-spots in plasmonic nanostructures taking advantage of their nonlinear response.[48,49]

Having determined the role played by the LSPRs at the pump frequency in TPL and SHG, we now turn our attention to their role at the emission step, i.e., at the emission frequency. The variation of TPL spectra with the spectral position of the LSPR is discussed first. The normalized TPL and dark-field scattering spectra for gold monomers as well as connected

DOI: 10.1021/acs.jpcc.6b04850
J. Phys. Chem. C 2016, 120, 17699−17710

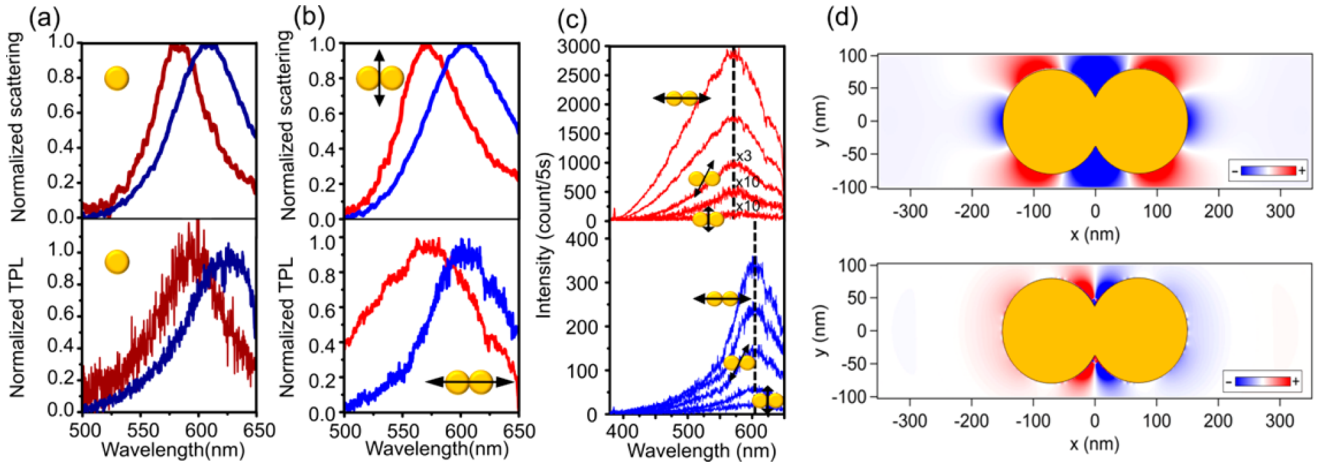

Figure 6. Normalized dark-field scattering spectra and TPL spectra for (a) monomers with diameters d = 80 nm (dark red) and d = 100 nm (dark blue) and for (b) connected dimers with disc diameters d = 80 nm (red) and d = 100 nm (blue). The directions of the incident polarization are indicated by the black arrows in panels b and c. (c) Nonlinear spectra of connected nanodimers with disc diameters d = 80 nm (red) and d = 100 nm (blue) for different incident polarization angles. The incident polarization was rotated from the short axis to the long axis of the dimers via 5 steps. To demonstrate the spectral changes clearly, the first three spectra for the dimer with disc diameter d = 80 nm are amplified by 10, 10, and 3 times, respectively. Excitation laser: 774 nm (110 fs, 89 MHz). Polarization: linearly polarized beam. (d) Real part of the x-component of the fundamental (top panel) and SH (bottom panel) fields in the vicinity of a connected gold dimer with a disc diameter d = 160 nm. The incident planewave is polarized along the long dimer axis.

dimers with different diameters are compared in Figure 6a,b, where the dark red and the dark blue lines correspond to monomers with disc diameters d = 80 and 100 nm, respectively, and the red and the blue lines represent connected dimers with disc diameters d = 80 and 100 nm, respectively. For both the monomers and connected dimers, the TPL spectral maximum shifts to longer wavelengths as the nanoparticle diameter increases. This trend is in agreement with the size-dependence of the LSPR changes shown in Figure 5c. Furthermore, it is interesting to note that, for the connected dimer excited with an incident wave polarized parallel to the long dimer axis, the maxima of the TPL spectra appear at the same wavelength as the transverse LSPR, as shown in Figure 6b. As further evidence of this effect, TPL spectra of the nanodimers have been recorded for different incident polarization angles, as shown in Figure 6c. Except for the magnitude of collected intensities, the TPL peak positions do not evolve with the incident polarization. Instead they match the scattering spectra obtained for an excitation polarized along the short dimer axis. These observations reveal the loss of coherence occurring in TPL due to the electron relaxation stage.[64] At this stage, the excited electrons achieve, after subpicosecond thermalization, a thermal equilibrium of the electronic population.[65−68] Subsequently, the energy is transferred to the cold lattice through electron−phonon and phonon−phonon couplings. The intermediate thermal nonequilibrium state of the electrons breaks up the direct connection between the excitation step and the radiative decay stage. This is one of the main reasons for losing the excitation polarization-dependence of the TPL spectra.[64] The other potential cause is the radiative decay process through the surface plasmon channel. This supplementary channel actually dominates the generation of photoluminescence from metallic nanoparticles, due to the efficient radiative decay rate of resonant plasmons, as reported in several previous studies.[13,69,70] For the connected dimers considered in this work, the transverse dipolar plasmon mode is mainly excited, explaining the similarity between the TPL spectra and the scattering spectra for an incident beam polarized along the short dimer axis.

Contrary to TPL, SHG does not express itself as a broad optical feature in the nonlinear spectra, but it corresponds to a narrow peak observed at the SH wavelength. This wavelength is directly related to the pump wavelength and does not depend on the LSPRs supported by the considered nanostructure. As a consequence, the influence of the LSPRs on SHG is different from that on TPL. Beyond the well-known enhancement occurring at the fundamental wavelength, when the incident wavelength matches that of a LSPR, SHG is also enhanced by the presence of a plasmonic mode at the emission wavelength, i.e., the SH wavelength. In other words, at the emission stage, the scattered SH signal is influenced only by the mode distribution at the SH wavelength.[71] To take advantage of this enhancement mechanism, researchers have designed doubly resonant plasmonic nanostructures, which are resonant at both the fundamental and SH wavelengths.[72−74] However, it is worth remembering that the parity of the SH modes differs from that of the fundamental excitation. Indeed, SHG is a three-photon process (involving two photons at the fundamental frequency and one photon at the SH frequency), and its selection rules differ from those of the linear response of plasmonic nanostructures. This difference is unambiguously revealed considering the parity of the involved modes. The near-field distribution of the fundamental electric field reveals that an odd (antisymmetric) mode is excited. Indeed, the vertical (0, y, z) plane is an antisymmetric plane for the fundamental near-field distributions (Figure 6d, top panel). However, the (0, y, z) plane is a symmetry plane for the SH electric field revealing that the SHG is described using an even (symmetric) mode (Figure 6d, bottom panel). This difference directly derives from the selection rules of SHG, which are based on its dependence upon centrosymmetry.[54] The connected dimers considered in this work are centrosymmetric, and a description of the SHG beyond the electric dipole approximation, i.e., including high order modes, is mandatory as previously emphasized in the case of spherical nano-

DOI: 10.1021/acs.jpcc.6b04850
J. Phys. Chem. C 2016, 120, 17699−17710

objects.[75] This is another difference with TPL, which is expected to be enhanced by bright plasmonic modes with high decay rate, as discussed in the previous paragraph. For both TPL and SHG, the LSPR enhancement at the emission stage is a key feature, important for the determination of the overall nonlinear conversion. This observation emphasizes again that the use of nonlinear optical processes for measuring the amplitude of electromagnetic hot-spots in plasmonic nanostructures requires significant care.

CONCLUSIONS

In this article, we have shown that the SHG and TPL signals originating from connected gold nanodimers depend in a different way on the excitation polarization, as a function of the dimer size. The SH intensity is maximal for an incident beam polarized along the long dimer axis for the smallest diameters (d = 80 and 100 nm), while it is maximal for an incident wave polarized perpendicularly to the long dimer axis for the largest diameters (d > 115 nm). On the contrary, the strongest TPL intensity is observed from the smallest dimer (with d = 80 nm), and for all the nanostructure sizes, the maximum TPL intensity is always found when an incident wave is polarized along the long dimer axis. Furthermore, for the connected dimers with disc diameters d = 80 and 100 nm, the maxima of the TPL spectra appear at the same wavelength as the transverse LSPR although they are excited with an incident wave polarized parallel to the long dimer axis. These intriguing experimental results, supported by numerical simulations, clearly demonstrate that TPL and SHG do not evolve in the same manner with the fundamental near-field distribution, which is controlled by the incident polarization angle. Our results clearly point out that the characterization of electromagnetic hot-spots using nonlinear optical processes is not straightforward, and that a competition between different contributions from parameters such as polarization, geometry, and resonance to the enhancement often occurs. These results provide new insights into the nonlinear optical properties of plasmonic systems, useful for the development of new applications in nonlinear plasmonics.

METHODS

Sample Fabrication. After being cleaned by acetone and isopropanol in an ultrasonic bath, the substrate (150 μm thick glass coverslip) was coated with a layer of electron-sensitive resist polymethylmethacrylate (PMMA) 950K diluted in methyl-iso-butylketone (MIBK) at 30g/L in a spin-coater (spinning speed, 3000 rpm; acceleration speed, 4000 rpm/s; duration, 30 s). The thickness of the resist is expected to be 160 nm, according to the empirical curve of the spinning speed versus the film thickness. After soft baking (convection oven at 170 °C for 3 h), we spin-coated a thin layer of conductive polymer (Espacer 300Z from Showa Denko Europe) to prevent charge accumulation during the exposure. Then, the resist was exposed with the predesigned patterns by the electron beam. After the conductive polymer was removed in water, the written patterns were developed via a solution of MIBK (diluted with isopropanol). In the development, the exposed areas of the resist were removed. Then, a physical vapor deposition (PVD) process was used to coat the sample with a 3 nm thick TiO_2 layer (for adhesion purposes) and a 50 nm thick Au layer. The sample was finally immersed in acetone for more than 3 h to lift off the remainder of the resist.

Linear Characterization Setup. Dark-field scattering spectroscopy was used to measure the linear optical properties of the connected gold dimers and of monomers for comparison. The sample, placed on an inverted microscope (Nikon Ti-U), was illuminated from the air side by a halogen lamp through a dark-field condenser (NA 0.8−0.95). The scattered light coming from the nanostructures was collected from the glass side by a 20× objective with a numerical aperture (NA) of 0.5 and sent to a spectrometer (Ocean Optics QE 65000) through a pinhole (200 μm diameter). The measured intensity curves were background corrected (using intensity curves measured in an unstructured area of the sample) and normalized by dividing by the (dark-current corrected) lamp spectrum.

Nonlinear Optical Setup. The nonlinear optical spectra of the plasmonic nanostructures were collected using a home-built confocal optical microscope. The optical path is shown in Figure S2 in the Supporting Information. A femtosecond laser generates ultrashort pulses (~110 fs, 89 MHz, 774 nm) and was employed to excite the sample. After a line filter and a gray filter, the beam passed through a λ-half wave plate, to be able to turn the linear polarization freely by 360°. Afterward the beam was expanded by two telescopes. By using a pinhole within the second telescope, undesired and scattered light was filtered out to obtain a homogeneous Gaussian mode. The linearly polarized light was reflected by a nonpolarizing dichroic beam splitter toward the parabolic mirror. The parabolic mirror serves both as the focusing element and the emission collector. In air its NA reaches 0.998.[76] Such a high-NA and low-chromatic-aberration mirror enables a high resolution down to the diffraction limit. The emitted optical signal of the nanoparticles was collected and sent through the beam splitter. The dichroic beam splitter excludes the light at the fundamental and higher wavelengths and only transmits the nonlinear information. After reducing the beam size with a third telescope, scattered light is excluded by a pinhole, and the detection wavelength range was selected by a band-pass filter (370−650 nm). With a flipping mirror, the beam was either directed toward the spectrometer (Princeton Instruments) to obtain spectral information or to an APD (single photon counting module, COUNT BLUE) for point-by-point imaging.

Once the expected pattern was found, a smaller scanning area was zoomed into, and the resolution was correspondingly optimized. The focus was always positioned at the center of the particle for the monomers; for the connected dimers, it was positioned at the center of the long axis. Turning the polarization of the excitation light via a λ-half wave plate in steps of 20° starting from the short axis of the dimers, spectra were recorded for each polarization (exposure time: 5 s). The SHG and TPL signal was extracted from each spectrum by integration over the wavelength ranges 380−390 and 390−650 nm, respectively. In the polarization-dependence measurements, the resulting intensity values were plotted for each excitation direction.

Linear Scattering Spectra Simulations. In order to simulate the dark-field experimental conditions, a volumic Green's tensor method was used.[77] In the model system, the dimer is located on a substrate of refractive index n = 1.5, excited by several polarized plane waves coming from the air side of the interface. The angle of incidence is θ = 63°, corresponding to the average angle of incidence through the dark-field condenser in the experiment. In order to take into account the finite numerical aperture for the collection of light,

DOI: 10.1021/acs.jpcc.6b04850
J. Phys. Chem. C 2016, 120, 17699−17710

the scattering spectra are computed by integrating the asymptotic Poynting vector in a cone of 20° around the normal to the interface in the glass (see Figure S5 in the Supporting Information). The contributions of two plane waves are incoherently summed for each polarization: in direction 1, the plane wave is incident at $\theta = 63°$, with the incidence plane being parallel to the dimer long axis; in direction 2, the plane wave is incident at $\theta = 63°$, with the incidence plane being perpendicular to the dimer long axis. Hence, for longitudinal illumination, the in-plane component of the p-polarization of direction 1 is summed with the s-polarization of direction 2. The same procedure is also performed for the transversal illumination, where the s-polarization of direction 1 is summed with the in-plane component of the p-polarization of direction 2. The geometric parameters used for the computation are derived from the SEM images of the connected dimers, which are $d = 80$ nm with a width at the constriction of 60 nm, $d = 100$ nm with a width of 65 nm, $d = 150$ nm with a width of 80 nm, and $d = 175$ nm with a width at the constriction of 85 nm.

Nonlinear Simulations. To disclose the physical origin of the TPL and SHG responses and explain the results of the experiments, numerical simulations were performed with an in-house SIE code giving accurate results for both the near- and the far-field distributions, even in resonant conditions.[78] Dispersive gold dielectric constants are extrapolated from experimental data.[79] The gold dimers are considered to be embedded in a homogeneous medium to reproduce the influence of the substrate on the surface plasmon resonances. The incident field is always described by a plane wave propagating along the z-axis. The linear response of the gold dimers is characterized by the backscattering evaluated 50 μm away from the plasmonic nanostructure. As the first step, the linear scattering spectra and the charge distributions are simulated using the SIE method to obtain the information on the local near-field strength. This information is then used for the computation of the SHG and TPL intensities. The assignment of the plasmonic modes excited at characteristic spectral positions is shown in Figure S6 in the Supporting Information, which is in very good agreement with the results shown in Figure 5.

Two distinct numerical schemes are used for the computation of the SHG and TPL responses. Let us first describe the SIE method for surface SHG. It is well-known that SHG is forbidden in the bulk of centrosymmetric media within the dipolar approximation.[80,81] Nevertheless, this symmetry is broken at the interface between two centrosymmetric media, and SHG arises from metallic nanostructure surfaces.[60,61] SIE methods only require the discretization of the surfaces of the metal nanoparticles, exactly where the SHG sources are located, and are therefore extremely well-suited for an accurate surface SHG computation.[80,81] Here we consider only the component of the surface tensor $\chi_{surf,\perp\perp\perp}$, where $\perp$ denotes the component normal to the surface, which is known to dominate the surface response for metallic nanoparticles.[60,61] In the present case, the nonlinear polarization can be written as $P_{surf,\perp}(\mathbf{r}, 2\omega) = \chi_{surf,\perp\perp\perp}E_n(\mathbf{r}, \omega)E_n(\mathbf{r}, \omega)$. The SH surface currents are obtained solving the SIE formulation taking into account the nonlinear polarization and enforcing the boundary conditions at the nanostructure surfaces. As the linear surface currents, the SH surface currents are expanded on Rao–Wilton–Glisson basis functions. The expansion coefficients are found applying the method of moments with Galerkin testing. A Poggio–Miller–Chang–Harrington–Wu–Tsai formulation is used to ensure accurate solutions even at resonant conditions.[78] The SH electric field is then deduced from the SH surface currents using a two-term subtraction method for the evaluation of the Green functions.[41,42] For comparison of the numerical results with the experimental observations, the SH intensity is integrated over a hemisphere reproducing the light collection performed by the parabolic mirror.

The approach used for the evaluation of the TPL signal is fundamentally different owing to its distinct physical origin. Contrary to SHG, which is a coherent surface process, TPL is a process involving the excitation of an electron–hole pair by the absorption of two incident photons, the relaxation of the excited electron and hole, and the emission of light due to the recombination of the electron with the hole.[28] The TPL intensity resulting from a pumping beam with a frequency ω_1 is given by[62]

$$I_{TPL} = \int \eta(\omega_2)|L^2(\omega_2)|\, d\omega_2 \cdot \iiint |E(r, \omega_1)|^4\, dV \quad (1)$$

where ω_2 is the TPL light frequency and $\eta(\omega_2)$ is the intrinsic luminescence yield of gold, which is related to its electronic band structure. $L(\omega_2)$ is the local field factor at the emission frequency, which is fixed to 1 in the present work for all the emission frequencies because we are only interested in the influence of the incident polarization on the TPL intensity. Indeed, this approximation neglects the effect of the surface plasmon resonance at the emission frequency, but not at the excitation stage.[70] In this framework, the first integral does not depend on the dimer geometry because all the dimers are made of gold. As a consequence, eq 1 can be rewritten as

$$I_{TPL} = A_{TPL} \iiint |E(r, \omega_1)|^4\, dV \quad (2)$$

We remain with the evaluation of the volume integral. All of the nanostructures considered in this work have the same thickness ($t = 40$ nm for the simulations). To compare the TPL intensity for different dimers and incident polarizations, the volume integral can be reduced to a 2D integration as[59,82]

$$I_{TPL} \propto \iint |E(r, \omega_1)|^4\, dx\, dy \quad (3)$$

where the integration is performed inside the nanostructure, in the symmetry plane ($z = 0$). Equation 3 is used to compute the TPL intensity for the different dimers and incident polarizations. Contrary to SHG, the TPL intensity is not evaluated in the far-field region, but is indeed proportional to the two-photon absorption cross section of the gold dimers.

■ ASSOCIATED CONTENT

Supporting Information

The Supporting Information is available free of charge on the ACS Publications website at DOI: 10.1021/acs.jpcc.6b04850.

Energy diagram of two-photon absorption, SEM image, sketch of optical setup, power-dependent photoluminescence intensity, phase information in the near-field, sketch of the illumination and signal collection schemes of the dark-field optical microscope, and linear simulation using surface integral equation (PDF)

■ AUTHOR INFORMATION

Corresponding Authors

*E-mail: pierre_michel.adam@utt.fr. Phone: +33 0325715661.

DOI: 10.1021/acs.jpcc.6b04850
J. Phys. Chem. C 2016, 120, 17699–17710

*E-mail: dai.zhang@uni-tuebingen.de. Phone: +49-7071-29-77639.

Notes

The authors declare no competing financial interest.

■ ACKNOWLEDGMENTS

This project is supported by the German Research Foundation DFG priority program SPP 1391 and by the German Academic Exchange Service DAAD through the program PPP France/PROCOPE. J.W. thanks the China Scholarship Council for supporting his research abroad. J.B. and O.J.F.M. acknowledge financial support from the Swiss National Science Foundation (SNSF, Project 200021_132694). A.H. acknowledges the support of the Institutional Strategy of the University of Tübingen (DFG ZUK63). The authors acknowledge the Region Champagne-Ardennes, the Conseil General de l'Aube, and the FEDER funds through their support of the nano-fabrication platform Nano'Mat. This work was performed in the context of the European COST Action MP1302 Nano-spectroscopy.

■ REFERENCES

(1) Kauranen, M.; Zayats, A. V. Nonlinear plasmonics. *Nat. Photonics* **2012**, *6*, 737−748.
(2) Maier, S. A. *Plasmonics: Fundamentals and Applications*; Springer Science + Business Media LLC: New York, 2007.
(3) Bharadwaj, P.; Deutsch, B.; Novotny, L. Optical antennas. *Adv. Opt. Photonics* **2009**, *1*, 438−483.
(4) Fang, Z.; Fan, L.; Lin, C.; Zhang, D.; Meixner, A. J.; Zhu, X. Plasmonic coupling of bow tie antennas with Ag nanowire. *Nano Lett.* **2011**, *11*, 1676−1680.
(5) Barnes, W. L.; Dereux, A.; Ebbesen, T. W. Surface plasmon subwavelength optics. *Nature* **2003**, *424*, 824−830.
(6) Howes, P. D.; Chandrawati, R.; Stevens, M. M. Colloidal nanoparticles as advanced biological sensors. *Science* **2014**, *346*, 53−53.
(7) Stockman, M. I. Nanoplasmonic sensing and detection. *Science* **2015**, *348*, 287−288.
(8) Acimovic, S. S.; Kreuzer, M. P.; González, M. U.; Quidant, R. Plasmon near-field coupling in metal dimers as a step toward single-molecule sensing. *ACS Nano* **2009**, *3*, 1231−1237.
(9) Ahn, T. K.; Avenson, T. J.; Ballottari, M.; Cheng, Y.-C.; Niyogi, K. K.; Bassi, R.; Fleming, G. R. Architecture of a charge-transfer state regulating light harvesting in a plant antenna protein. *Science* **2008**, *320*, 794−797.
(10) Hofmann, E.; Wrench, P. M.; Sharples, F. P.; Hiller, R. G.; Welte, W.; Diederichs, K. Structural basis of light harvesting by carotenoids: peridinin-chlorophyll-protein from Amphidinium carterae. *Science* **1996**, *272*, 1788−1791.
(11) Lin, J.; Li, H.; Zhang, H.; Chen, W. Plasmonic enhancement of photocurrent in MoS2 field-effect-transistor. *Appl. Phys. Lett.* **2013**, *102*, 203109.
(12) Guo, N.; Hu, W.-D.; Chen, X.-S.; Wang, L.; Lu, W. Enhanced plasmonic resonant excitation in a grating gated field-effect transistor with supplemental gates. *Opt. Express* **2013**, *21*, 1606−1614.
(13) Horneber, A.; Braun, K.; Rogalski, J.; Leiderer, P.; Meixner, A. J.; Zhang, D. Nonlinear optical imaging of single plasmonic nanoparticles with 30 nm resolution. *Phys. Chem. Chem. Phys.* **2015**, *17*, 21288−21293.
(14) Jäger, S.; Kern, A. M.; Hentschel, M.; Jäger, R.; Braun, K.; Zhang, D.; Giessen, H.; Meixner, A. J. Au nanotip as luminescent near-field probe. *Nano Lett.* **2013**, *13*, 3566−3570.
(15) Novotny, L.; Van Hulst, N. Antennas for light. *Nat. Photonics* **2011**, *5*, 83−90.
(16) Viste, P.; Plain, J.; Jaffiol, R.; Vial, A.; Adam, P. M.; Royer, P. Enhancement and quenching regimes in metal−semiconductor hybrid optical nanosources. *ACS Nano* **2010**, *4*, 759−764.
(17) Lal, S.; Link, S.; Halas, N. J. Nano-optics from sensing to waveguiding. *Nat. Photonics* **2007**, *1*, 641−648.
(18) Halas, N. J.; Lal, S.; Chang, W.-S.; Link, S.; Nordlander, P. Plasmons in strongly coupled metallic nanostructures. *Chem. Rev.* **2011**, *111*, 3913−3961.
(19) Wen, F.; Zhang, Y.; Gottheim, S.; King, N. S.; Zhang, Y.; Nordlander, P.; Halas, N. J. Charge transfer plasmons: optical frequency conductances and tunable infrared resonances. *ACS Nano* **2015**, *9*, 6428−6435.
(20) Grand, J.; Adam, P.-M.; Grimault, A.-S.; Vial, A.; De La Chapelle, M. L.; Bijeon, J.-L.; Kostcheev, S.; Royer, P. Optical extinction spectroscopy of oblate, prolate and ellipsoid shaped gold nanoparticles: experiments and theory. *Plasmonics* **2006**, *1*, 135−140.
(21) Nordlander, P.; Oubre, C.; Prodan, E.; Li, K.; Stockman, M. Plasmon hybridization in nanoparticle dimers. *Nano Lett.* **2004**, *4*, 899−903.
(22) Russell, K. J.; Liu, T.-L.; Cui, S.; Hu, E. L. Large spontaneous emission enhancement in plasmonic nanocavities. *Nat. Photonics* **2012**, *6*, 459−462.
(23) Knight, M. W.; Sobhani, H.; Nordlander, P.; Halas, N. J. Photodetection with active optical antennas. *Science* **2011**, *332*, 702−704.
(24) Gaiduk, A.; Yorulmaz, M.; Orrit, M. Correlated absorption and photoluminescence of single gold nanoparticles. *ChemPhysChem* **2011**, *12*, 1536−1541.
(25) Konrad, A.; Wackenhut, F.; Hussels, M.; Meixner, A. J.; Brecht, M. Temperature dependent luminescence and dephasing of gold nanorods. *J. Phys. Chem. C* **2013**, *117*, 21476−21482.
(26) Wackenhut, F.; Failla, A. V.; Züchner, T.; Steiner, M.; Meixner, A. J. Three-dimensional photoluminescence mapping and emission anisotropy of single gold nanorods. *Appl. Phys. Lett.* **2012**, *100*, 263102.
(27) Crut, A.; Maioli, P.; Del Fatti, N.; Vallée, F. Optical absorption and scattering spectroscopies of single nano-objects. *Chem. Soc. Rev.* **2014**, *43*, 3921−3956.
(28) Boyd, G.; Yu, Z.; Shen, Y. Photoinduced luminescence from the noble metals and its enhancement on roughened surfaces. *Phys. Rev. B: Condens. Matter Mater. Phys.* **1986**, *33*, 7923−7936.
(29) Wilcoxon, J.; Martin, J.; Parsapour, F.; Wiedenman, B.; Kelley, D. Photoluminescence from nanosize gold clusters. *J. Chem. Phys.* **1998**, *108*, 9137−9143.
(30) Dulkeith, E.; Niedereichholz, T.; Klar, T.; Feldmann, J.; Von Plessen, G.; Gittins, D.; Mayya, K.; Caruso, F. Plasmon emission in photoexcited gold nanoparticles. *Phys. Rev. B: Condens. Matter Mater. Phys.* **2004**, *70*, 205424.
(31) Kinkhabwala, A.; Yu, Z.; Fan, S.; Avlasevich, Y.; Müllen, K.; Moerner, W. Large single-molecule fluorescence enhancements produced by a bowtie nanoantenna. *Nat. Photonics* **2009**, *3*, 654−657.
(32) Ye, J.; Wen, F.; Sobhani, H.; Lassiter, J. B.; Dorpe, P. V.; Nordlander, P.; Halas, N. J. Plasmonic nanoclusters: near field properties of the Fano resonance interrogated with SERS. *Nano Lett.* **2012**, *12*, 1660−1667.
(33) Nie, S.; Emory, S. R. Probing single molecules and single nanoparticles by surface-enhanced Raman scattering. *Science* **1997**, *275*, 1102−1106.
(34) Martin, J.; Kociak, M.; Mahfoud, Z.; Proust, J.; Gérard, D.; Plain, J. High-resolution imaging and spectroscopy of multipolar plasmonic resonances in aluminum nanoantennas. *Nano Lett.* **2014**, *14*, 5517−5523.
(35) Duan, H.; Fernández-Domínguez, A. I.; Bosman, M.; Maier, S. A.; Yang, J. K. Nanoplasmonics: classical down to the nanometer scale. *Nano Lett.* **2012**, *12*, 1683−1689.
(36) Butet, J.; Brevet, P.-F.; Martin, O. J. F. Optical second harmonic generation in plasmonic nanostructures: from fundamental principles to advanced applications. *ACS Nano* **2015**, *9*, 10545−10562.

DOI: 10.1021/acs.jpcc.6b04850
J. Phys. Chem. C 2016, 120, 17699−17710

(37) Reichenbach, P.; Horneber, A.; Gollmer, D. A.; Hille, A.; Mihaljevic, J.; Schäfer, C.; Kern, D. P.; Meixner, A. J.; Zhang, D.; Fleischer, M. Nonlinear optical point light sources through field enhancement at metallic nanocones. *Opt. Express* **2014**, *22*, 15484−15501.
(38) Hajisalem, G.; Nezami, M. S.; Gordon, R. Probing the quantum tunneling limit of plasmonic enhancement by third harmonic generation. *Nano Lett.* **2014**, *14*, 6651−6654.
(39) Horneber, A.; Baudrion, A.-L.; Adam, P.-M.; Meixner, A. J.; Zhang, D. Compositional-asymmetry influenced non-linear optical processes of plasmonic nanoparticle dimers. *Phys. Chem. Chem. Phys.* **2013**, *15*, 8031−8034.
(40) Farrer, R. A.; Butterfield, F. L.; Chen, V. W.; Fourkas, J. T. Highly efficient multiphoton-absorption-induced luminescence from gold nanoparticles. *Nano Lett.* **2005**, *5*, 1139−1142.
(41) Bouhelier, A.; Beversluis, M.; Hartschuh, A.; Novotny, L. Near-field second-harmonic generation induced by local field enhancement. *Phys. Rev. Lett.* **2003**, *90*, 013903.
(42) Danckwerts, M.; Novotny, L. Optical frequency mixing at coupled gold nanoparticles. *Phys. Rev. Lett.* **2007**, *98*, 026104.
(43) Butet, J.; Duboisset, J.; Bachelier, G.; Russier-Antoine, I.; Benichou, E.; Jonin, C.; Brevet, P.-F. Optical second harmonic generation of single metallic nanoparticles embedded in a homogeneous medium. *Nano Lett.* **2010**, *10*, 1717−1721.
(44) Hentschel, M.; Utikal, T.; Giessen, H.; Lippitz, M. Quantitative modeling of the third harmonic emission spectrum of plasmonic nanoantennas. *Nano Lett.* **2012**, *12*, 3778−3782.
(45) Zhang, Y.; Grady, N. K.; Ayala-Orozco, C.; Halas, N. J. Three-dimensional nanostructures as highly efficient generators of second harmonic light. *Nano Lett.* **2011**, *11*, 5519−5523.
(46) Husu, H.; Siikanen, R.; Mäkitalo, J.; Lehtolahti, J.; Laukkanen, J.; Kuittinen, M.; Kauranen, M. Metamaterials with tailored nonlinear optical response. *Nano Lett.* **2012**, *12*, 673−677.
(47) Mühlschlegel, P.; Eisler, H.-J.; Martin, O. J. F.; Hecht, B.; Pohl, D. Resonant optical antennas. *Science* **2005**, *308*, 1607−1609.
(48) Ghenuche, P.; Cherukulappurath, S.; Taminiau, T. H.; van Hulst, N. F.; Quidant, R. Spectroscopic mode mapping of resonant plasmon nanoantennas. *Phys. Rev. Lett.* **2008**, *101*, 116805.
(49) Shen, S.; Meng, L.-Y.; Zhang, Y.; Han, J.; Ma, Z.; Hu, S.; He, Y.; Li, J.-F.; Ren, B.; Shih, T.-M.; et al. Plasmon-enhanced second-harmonic generation nanorulers with ultrahigh sensitivities. *Nano Lett.* **2015**, *15*, 6716−6721.
(50) Black, L.-J.; Wiecha, P. R.; Wang, Y.; de Groot, C.; Paillard, V.; Girard, C.; Muskens, O. L.; Arbouet, A. Tailoring Second Harmonic Generation in single L-shaped plasmonic nanoantennas from the capacitive to conductive coupling regime. *ACS Photonics* **2015**, *2*, 1592−1601.
(51) Butet, J.; Thyagarajan, K.; Martin, O. J. F. Ultrasensitive optical shape characterization of gold nanoantennas using second harmonic generation. *Nano Lett.* **2013**, *13*, 1787−1792.
(52) Slablab, A.; Le Xuan, L.; Zielinski, M.; de Wilde, Y.; Jacques, V.; Chauvat, D.; Roch, J.-F. Second-harmonic generation from coupled plasmon modes in a single dimer of gold nanospheres. *Opt. Express* **2012**, *20*, 220−227.
(53) Berthelot, J.; Bachelier, G.; Song, M.; Rai, P.; Colas des Francs, G.; Dereux, A.; Bouhelier, A. Silencing and enhancement of second-harmonic generation in optical gap antennas. *Opt. Express* **2012**, *20*, 10498−10508.
(54) Butet, J.; Dutta-Gupta, S.; Martin, O. J. F. Surface second-harmonic generation from coupled spherical plasmonic nanoparticles: Eigenmode analysis and symmetry properties. *Phys. Rev. B: Condens. Matter Mater. Phys.* **2014**, *89*, 245449.
(55) Canfield, B. K.; Husu, H.; Laukkanen, J.; Bai, B.; Kuittinen, M.; Turunen, J.; Kauranen, M. Local field asymmetry drives second-harmonic generation in noncentrosymmetric nanodimers. *Nano Lett.* **2007**, *7*, 1251−1255.
(56) Jiang, X.-F.; Pan, Y.; Jiang, C.; Zhao, T.; Yuan, P.; Venkatesan, T.; Xu, Q.-H. Excitation nature of two-photon photoluminescence of gold nanorods and coupled gold nanoparticles studied by two-pulse emission modulation spectroscopy. *J. Phys. Chem. Lett.* **2013**, *4*, 1634−1638.
(57) Viarbitskaya, S.; Demichel, O.; Cluzel, B.; Colas des Francs, G.; Bouhelier, A. Delocalization of nonlinear optical responses in plasmonic nanoantennas. *Phys. Rev. Lett.* **2015**, *115*, 197401.
(58) Biagioni, P.; Celebrano, M.; Savoini, M.; Grancini, G.; Brida, D.; Mátéfi-Tempfli, S.; Mátéfi-Tempfli, M.; Duò, L.; Hecht, B.; Cerullo, G. Dependence of the two-photon photoluminescence yield of gold nanostructures on the laser pulse duration. *Phys. Rev. B: Condens. Matter Mater. Phys.* **2009**, *80*, 045411.
(59) Castro-Lopez, M.; Brinks, D.; Sapienza, R.; van Hulst, N. F. Aluminum for nonlinear plasmonics: resonance-driven polarized luminescence of Al, Ag, and Au nanoantennas. *Nano Lett.* **2011**, *11*, 4674−4678.
(60) Wang, F. X.; Rodríguez, F. J.; Albers, W. M.; Ahorinta, R.; Sipe, J.; Kauranen, M. Surface and bulk contributions to the second-order nonlinear optical response of a gold film. *Phys. Rev. B: Condens. Matter Mater. Phys.* **2009**, *80*, 233402.
(61) Bachelier, G.; Butet, J.; Russier-Antoine, I.; Jonin, C.; Benichou, E.; Brevet, P.-F. Origin of optical second-harmonic generation in spherical gold nanoparticles: Local surface and nonlocal bulk contributions. *Phys. Rev. B: Condens. Matter Mater. Phys.* **2010**, *82*, 235403.
(62) Wang, D.-S.; Hsu, F.-Y.; Lin, C.-W. Surface plasmon effects on two photon luminescence of gold nanorods. *Opt. Express* **2009**, *17*, 11350−11359.
(63) Husu, H.; Canfield, B. K.; Laukkanen, J.; Bai, B.; Kuittinen, M.; Turunen, J.; Kauranen, M. Local-field effects in the nonlinear optical response of metamaterials. *Metamaterials* **2008**, *2*, 155−168.
(64) Shahbazyan, T. V. Theory of plasmon-enhanced metal photoluminescence. *Nano Lett.* **2013**, *13*, 194−198.
(65) Link, S.; Burda, C.; Wang, Z. L.; El-Sayed, M. A. Electron dynamics in gold and gold−silver alloy nanoparticles: The influence of a nonequilibrium electron distribution and the size dependence of the electron−phonon relaxation. *J. Chem. Phys.* **1999**, *111*, 1255−1264.
(66) Sun, C.-K.; Vallée, F.; Acioli, L.; Ippen, E.; Fujimoto, J. Femtosecond-tunable measurement of electron thermalization in gold. *Phys. Rev. B: Condens. Matter Mater. Phys.* **1994**, *50*, 15337.
(67) Hohlfeld, J.; Wellershoff, S.-S.; Güdde, J.; Conrad, U.; Jähnke, V.; Matthias, E. Electron and lattice dynamics following optical excitation of metals. *Chem. Phys.* **2000**, *251*, 237−258.
(68) Zavelani-Rossi, M.; Polli, D.; Kochtcheev, S.; Baudrion, A.-L.; Béal, J.; Kumar, V.; Molotokaite, E.; Marangoni, M.; Longhi, S.; Cerullo, G.; et al. Transient optical response of a single gold nanoantenna: the role of plasmon detuning. *ACS Photonics* **2015**, *2*, 521−529.
(69) Hu, H.; Duan, H.; Yang, J. K.; Shen, Z. X. Plasmon-modulated photoluminescence of individual gold nanostructures. *ACS Nano* **2012**, *6*, 10147−10155.
(70) Bouhelier, A.; Bachelot, R.; Lerondel, G.; Kostcheev, S.; Royer, P.; Wiederrecht, G. Surface plasmon characteristics of tunable photoluminescence in single gold nanorods. *Phys. Rev. Lett.* **2005**, *95*, 267405.
(71) Metzger, B.; Gui, L.; Fuchs, J.; Floess, D.; Hentschel, M.; Giessen, H. Strong enhancement of second harmonic emission by plasmonic resonances at the second harmonic wavelength. *Nano Lett.* **2015**, *15*, 3917−3922.
(72) Thyagarajan, K.; Rivier, S.; Lovera, A.; Martin, O. J. F. Enhanced second-harmonic generation from double resonant plasmonic antennae. *Opt. Express* **2012**, *20*, 12860−12865.
(73) Aouani, H.; Navarro-Cia, M.; Rahmani, M.; Sidiropoulos, T. P.; Hong, M.; Oulton, R. F.; Maier, S. A. Multiresonant broadband optical antennas as efficient tunable nanosources of second harmonic light. *Nano Lett.* **2012**, *12*, 4997−5002.
(74) Celebrano, M.; Wu, X.; Baselli, M.; Großmann, S.; Biagioni, P.; Locatelli, A.; De Angelis, C.; Cerullo, G.; Osellame, R.; Hecht, B.; et al. Mode matching in multiresonant plasmonic nanoantennas for enhanced second harmonic generation. *Nat. Nanotechnol.* **2015**, *10*, 412−417.

DOI: 10.1021/acs.jpcc.6b04850
J. Phys. Chem. C 2016, 120, 17699−17710

(75) Dadap, J. I.; Shan, J.; Eisenthal, K. B.; Heinz, T. F. Second-harmonic Rayleigh scattering from a sphere of centrosymmetric material. *Phys. Rev. Lett.* **1999**, *83*, 4045.
(76) Lieb, M.; Meixner, A. A high numerical aperture parabolic mirror as imaging device for confocal microscopy. *Opt. Express* **2001**, *8*, 458−474.
(77) Paulus, M.; Gay-Balmaz, P.; Martin, O. J. F. Accurate and efficient computation of the Green's tensor for stratified media. *Phys. Rev. E: Stat. Phys., Plasmas, Fluids, Relat. Interdiscip. Top.* **2000**, *62*, 5797.
(78) Kern, A. M.; Martin, O. J. F. Surface integral formulation for 3D simulations of plasmonic and high permittivity nanostructures. *J. Opt. Soc. Am. A* **2009**, *26*, 732−740.
(79) Johnson, P. B.; Christy, R.-W. Optical constants of the noble metals. *Phys. Rev. B* **1972**, *6*, 4370−4379.
(80) Butet, J.; Gallinet, B.; Thyagarajan, K.; Martin, O. J. F. Second-harmonic generation from periodic arrays of arbitrary shape plasmonic nanostructures: a surface integral approach. *J. Opt. Soc. Am. B* **2013**, *30*, 2970−2979.
(81) Mäkitalo, J.; Suuriniemi, S.; Kauranen, M. Boundary element method for surface nonlinear optics of nanoparticles. *Opt. Express* **2011**, *19*, 23386−23399.
(82) Schuck, P.; Fromm, D.; Sundaramurthy, A.; Kino, G.; Moerner, W. Improving the mismatch between light and nanoscale objects with gold bowtie nanoantennas. *Phys. Rev. Lett.* **2005**, *94*, 017402.

DOI: 10.1021/acs.jpcc.6b04850
J. Phys. Chem. C 2016, 120, 17699−17710